

¹ Fourier Neural Operators for Accelerating Earthquake
² Dynamic Rupture Simulations

³ **Napat Tainpkdipat** ¹, **Mohamed Abdelmeguid** ², **Chunhui Zhao** ¹, **Kamyar**
⁴ **Azizzadenesheli** ³, **Ahmed Elbanna** ^{1,4}

⁵ Department of Civil and Environmental Engineering, University of Illinois Urbana Champaign, Urbana,
⁶ IL 61801, USA.

⁷ Graduate Aerospace Laboratories, California Institute of Technology, Pasadena, CA 91125, USA.

⁸ ³Nvidia Corporation, Santa Clara, CA 95051, USA.

⁹ Beckman Institute of Advanced Science and Technology, University of Illinois Urbana Champaign,
¹⁰ Urbana, IL 61801, USA.

¹¹ **Key Points:**

- ¹² We develop a Fourier Neural Operator (FNO) framework to simulate earthquake
rupture under varying fractal stress and friction.
- ¹³ The FNO achieves up to 4×10^5 times speedup compared to the Spectral Bound-
ary Integral method.
- ¹⁴ We demonstrate that the model can generalize to unseen shear stress and frictional
parameters, including out-of-distribution cases.

18 **Abstract**

19 Dynamic rupture modeling plays a crucial role in unraveling earthquake source processes.
20 However, the multiscale nature of rupture propagation pose significant challenges, and
21 classical numerical methods remain computationally expensive. To overcome this hur-
22 dle, we present a methodology that is both computationally efficient and quantitatively
23 accurate. Specifically, we introduce a surrogate model, in the form of a Fourier Neural
24 Operator, for emulating the nonlinear equations governing dynamic rupture propaga-
25 tion on frictional interfaces. This surrogate is trained on synthetic data generated by mul-
26 tiple physics-based dynamic rupture simulations and is then applied to unseen problems.
27 The proposed methodology retains the accuracy of traditional multiscale methods at a
28 significantly reduced computational cost, achieving a speedup of up to 4×10^5 compared
29 to the state-of-the—art conventional methods. We evaluate this approach using various
30 examples and demonstrate its efficacy in capturing the spacetime evolution of fault slip
31 rates for a wide range of stress conditions. This development advances the state of the
32 art of computational earthquake dynamics and opens new opportunities for accelerat-
33 ing physics-based rupture forecasts.

34 **Plain Language Summary**

35 Earthquakes begin when stress builds up and causes sudden movement along faults
36 in the Earth’s crust. To simulate how an earthquake spreads, traditional numerical mod-
37 els are often used. However, these models can be computationally intensive and time-
38 consuming due to the complexity of earthquake processes. This study introduces a faster
39 way to model earthquakes using a machine learning tool, specifically a Fourier Neural
40 Operator framework. The model learns patterns from previous earthquake simulations
41 and uses that knowledge to predict how a fault slips under different stress and friction
42 conditions. This approach achieves a speedup of up to 4×10^5 times compared to tra-
43 ditional methods, potentially enabling the rapid exploration of many scenarios and im-
44 proving the ability to study and forecast earthquakes efficiently.

45 **1 Introduction**

46 Earthquakes are among the most destructive natural hazards, yet available data
47 remains limited. Large earthquake events are rare, and their recorded histories are short,
48 posing challenges for purely data-driven analyses. Furthermore, because earthquakes orig-
49 inate at depths where direct measurements are impossible, observations rely on sparse
50 surface instrumentation, offering an incomplete view of fault dynamics (Arrowsmith et
51 al., 2022). Earthquake modeling is therefore essential to interpret limited observations
52 and infer subsurface processes that cannot be directly measured (Nielsen et al., 2000; Duan
53 & Oglesby, 2006; Bhat et al., 2007; Ma & Elbanna, 2019; Ripperger et al., 2007; Gabriel
54 et al., 2012; Xu et al., 2015).

55 Modeling earthquakes is inherently challenging, as it requires integrating data from
56 multiple sources, including field observations and laboratory experiments, with physics-
57 based simulations.(Johnson et al., 2006; Gallović et al., 2019a, 2019b; Aochi & Twardzik,
58 2020; Van Zelst et al., 2019). Additionally, key fault properties remain uncertain since
59 they cannot be directly measured. The multiscale nature of earthquakes further com-
60 plicates the problem. The rupture occurs within seconds, but the recurrence intervals
61 span years to centuries. Physically, earthquakes propagate over kilometers, whereas the
62 rupture process zone might be confined to a few meters (Lapusta et al., 2000; Ben-Zion,
63 2008; Chester & Chester, 1998). Accurately capturing rupture dynamics requires extremely
64 fine discretization, often at the sub-meter scale, leading to immense computational costs
65 (Ulrich et al., 2019).

Traditional numerical methods such as the finite element method (FEM) (Oglesby et al., 1998, 2000; Aagaard et al., 2001), finite difference method (FDM) (Andrews, 1973; Day, 1982; Madariaga et al., 1998; Andrews, 1999; Dalguer & Day, 2007; Moczo et al., 2007), and boundary integral methods (BIM) (Das, 1980; Andrews, 1985; Cochard & Madariaga, 1994; Geubelle & Rice, 1995) have been widely used for earthquake simulations . Recent advances focus on reducing computational costs while maintaining accuracy, including hybrid approaches like the finite element–spectral boundary integral method (Ma et al., 2019; Abdelmeguid et al., 2019; Abdelmeguid & Elbanna, 2022). However, despite these advances, the primary bottleneck in dynamic rupture modeling remains the inherent computational intensity, especially in the context of dynamic inversion for fault stress and friction. Each inversion requires solving the equations governing fault slip across a wide range of possible initial conditions, material properties, and frictional parameters, often necessitating large number of forward model evaluations. Therefore, developing more efficient approaches remains essential to overcome these computational challenges. Rapid simulations allow the study of fault behavior under varying conditions. They also enable large-scale statistical analyses, helping to identify rare or extreme events, which are essential for seismic hazard assessment. Additionally, accelerated accurate simulations reduce the computational burden of traditional methods, making large-scale inverse analyses more feasible.

In recent years, machine learning methods have emerged as a powerful tool for addressing these computational challenges in various domains, including seismology (Zhu et al., 2019; L. Yang et al., 2022; Zhu & Beroza, 2019; Mousavi et al., 2020; Ross et al., 2018, 2019; Zhu et al., 2022). Deep learning approaches, specifically neural operators, have shown promise in approximating solutions to partial differential equations (PDEs), which govern many physical processes (Kovachki et al., 2023; Azizzadenesheli et al., 2024; Rahman et al., 2022). Unlike traditional neural networks, which map finite-dimensional input vectors to output vectors, neural operators learn mappings between entire functions. This capability allows them to solve complex problems governed by PDEs without requiring retraining, enabling rapid and efficient solution generation.

In seismology, neural operators have been applied to 2D acoustic wave equation (B. Li et al., 2023; Y. Yang et al., 2021), the elastic wave equation (Lehmann et al., 2023, 2024; Zou et al., 2024; Zhang et al., 2023), viscoelastic wave models (Wei & Fu, 2022), and full-waveform inversion (Y. Yang et al., 2023). While these applications have demonstrated the effectiveness of neural operators in handling wave propagation and seismic inversion tasks, their potential for modeling dynamic rupture propagation remains unexplored.

Dynamic rupture modeling presents unique challenges for machine learning due to the highly nonlinear and multiscale nature of fault slip processes. Capturing the evolution of rupture fronts, where stresses and slip rates exhibit sharp gradients, requires fine spatial and temporal resolution, leading to high computational costs. One potential approach that can address such challenges is Fourier Neural Operators (FNOs) (Z. Li et al., 2020). Through spectral representation in Fourier space, FNOs efficiently capture long-range correlations and high-dimensional dependencies. By adding more Fourier modes, it is also possible to capture increasingly higher frequencies. Moreover, their superior trade-off between computational cost and accuracy makes them well-suited for this problem (de Hoop et al., 2022).

Here, we present a framework for accelerating earthquake dynamic rupture simulations using FNOs. We use FNOs to generate the full spatio-temporal evolution of the fault slip rate. The proposed approach leverages the efficiency and accuracy of FNOs to address the large computational demands required by physics-based numerical methods. Specifically, we train FNOs on synthetic datasets incorporating heterogeneous distributions of initial shear stress and frictional parameters. The performance of the FNO framework is evaluated across various datasets, demonstrating its ability to generalize and accurately predict fault slip dynamics with significant computational speedup.

119 The remainder of the paper is organized as follows. In Section 2 we give an overview
 120 of FNOs and describe the dynamic rupture problem setup. We discuss the nature of the
 121 different datasets used in training the model in Section 3. We summarize our results in
 122 Section 4. We discuss the implications of our findings and summarize our conclusions
 123 in Section 5.

124 2 Preliminaries and Problem Setup

125 2.1 Fourier Neural Operators

126 The Fourier Neural Operator (FNO) is a learning-based operator designed to map
 127 between infinite-dimensional spaces using input-output pairs, $\{a_j, u_j\}_{j=1}^N$. FNO replaces
 128 the kernel integral operator in traditional neural operators with a convolution operator
 129 defined in Fourier space. Subsequently, an inverse Fourier transform is applied, along with
 130 a linear transformation. The resulting values are then passed through an activation func-
 131 tion, which is applied to the sum of the transformed features. Mathematically, the neu-
 132 ral operator follows an iterative update process, $v_0 \rightarrow v_1 \rightarrow v_2 \rightarrow \dots \rightarrow v_T$, where
 133 the update from v_0 to v_M and the output $u(x)$ are defined as follows:

$$v_0(x) = P(a(x)) \\ v_{m+1}(x) = \sigma \left(W_m v_m(x) + \int k(x, y)_m v_m(y) dy \right), \quad m = 0, \dots, M-1 \\ u(x) = Q(v_M(x)) \quad (1)$$

134 where P is a pointwise lifting operator parameterized with a neural network that
 135 projects the point values of input function $a(x)$ to a higher dimension. W_m is a linear
 136 transformation applied to $v_m(x)$ to account for non-periodic boundary conditions. $\int k(x, y)v_m(y), dy$
 137 represents a kernel integral operator. Q is a pointwise projection operator parameter-
 138 ized with a neural network that maps back to the target dimension. σ is a nonlinear ac-
 139 tivation function.

140 In FNO, we replace the kernel integral operator with a convolution operator us-
 141 ing the fast Fourier transform. Thus, we can rewrite the kernel integral operator as fol-
 142 lows:

$$\int k(x, y)_m v_m(y) dy = \mathcal{F}^{-1}(\mathcal{F}(k_m) \cdot \mathcal{F}(v_m)) \quad (2)$$

143 where \mathcal{F} and \mathcal{F}^{-1} are the Fourier transform and its inverse, respectively. Using the
 144 Fourier transform enhances computational efficiency, allows the model to handle global
 145 dependencies, and enables resolution invariance, meaning the model can generalize across
 146 different spatial and temporal resolutions without requiring retraining. Specifically, when
 147 the input function is provided in regular grids, the Fourier transformer is carried using
 148 fast Fourier transform, a celebrated and fast algorithm for Fourier analysis. It also leads
 149 to better generalization across grids, reduces computational costs for high-dimensional
 150 problems, and improves the model's ability to handle complex, nonlinear dynamics. We
 151 refer the reader to (Z. Li et al., 2020) for a discussion of this architecture and related fea-
 152 tures.

153 2.2 Fault Model Setup

154 We consider a two-dimensional (2D) planar fault embedded in a three-dimensional
 155 (3D) homogeneous, isotropic, and elastic domain Ω . The domain includes a traction bound-
 156 ary Γ_T , a displacement boundary Γ_u , and a fault surface located along Γ_f . We adopt

157 the TPV101 benchmark problem setup from the SCEC/USGS dynamic earthquake rup-
 158 ture code verification exercise (Harris et al., 2018, 2009; Kammer et al., 2021). The gov-
 159 erning equations are given by:

$$\rho \frac{\partial^2 u_i}{\partial t^2} - \frac{\partial \sigma_{ij}}{\partial x_j} - b_i = 0 \quad \text{in } \Omega, \quad (3)$$

$$\sigma_{ij} n_j = T_i \quad \text{on } \Gamma_T, \quad (4)$$

$$u_i = u_i^0 \quad \text{on } \Gamma_u, \quad (5)$$

$$(u_i^+ - u_i^-) = \delta_i, \quad T_{f,i}^+ = -T_{f,i}^- \quad \text{on } \Gamma_f. \quad (6)$$

160 Here, ρ is the density, u_i represents the displacement vector, b_i denotes the body
 161 force vector, and δ_i is the slip. The superscripts + and - refer to the positive and neg-
 162 ative sides of the fault, respectively. The stress-strain relationship can be defined by lin-
 163 ear elasticity:

$$\sigma_{ij} = \lambda \delta_{ij} \epsilon_{kk} + 2\mu \epsilon_{ij}, \quad (7)$$

164 where λ and μ are the Lamé parameters, δ_{ij} is the Kronecker delta, and ϵ_{ij} is the
 165 strain tensor. The domain is characterized by its density (ρ), shear wave speed (c_s), and
 166 pressure wave speed (c_p), as summarized in Table 1.

167 The shear component of the fault boundary condition is governed by a regularized
 168 rate-and-state friction law with an aging formulation (Dieterich, 1979; Ruina, 1983; Ben-
 169 Zion & Rice, 1997; Lapusta et al., 2000; Ampuero & Rubin, 2008). This formulation re-
 170 lates the fault's strength to the slip rate (V), normal stress (σ), and state variable (θ)
 171 through the following equations.

$$\tau = a\sigma \operatorname{arcsinh} \left[\frac{V}{2V^*} \exp \left(\frac{f^* + b \ln(V^* \theta / D_{RS})}{a} \right) \right], \quad (8)$$

172 In expression (8), the parameter combination of a , and b dictates the stability of
 173 the frictional interface. $a-b > 0$ corresponds to a steady state rate-strengthening fric-
 174 tional response (VS) in which sliding is stable. In contrast, $a-b < 0$ corresponds to a
 175 steady state rate-weakening frictional response (VW) which may lead to unstable slip
 176 and stick-slip sequences.

$$\frac{d\theta}{dt} = 1 - \frac{V\theta}{D_{RS}}. \quad (9)$$

177 A schematic representation of the fault geometry is shown in Figure 1a. The hypocen-
 178 ter is located at $(x_0, y_0) = (0, 0)$ km. The fault consists of a central velocity-weakening
 179 (VW) regime, defined by $-W < x < W$ and $-W/2 < y < W/2$, with $W = 15$ km.
 180 This region defines the boundaries of the seismogenic zone which is characterized by a
 181 negative value of $a-b$. Surrounding the VW region is a velocity-strengthening (VS) regime,
 182 which is characterized by a positive value of $a-b$, with a transition layer of width $w =$
 183 3 km. To ensure a smooth transition between these regions, the parameter a varies smoothly
 184 based on a mathematically smoothed version of the boxcar function. The variation in
 185 a is governed by:

$$a = a_0 + \Delta a(x, y), \quad (10)$$

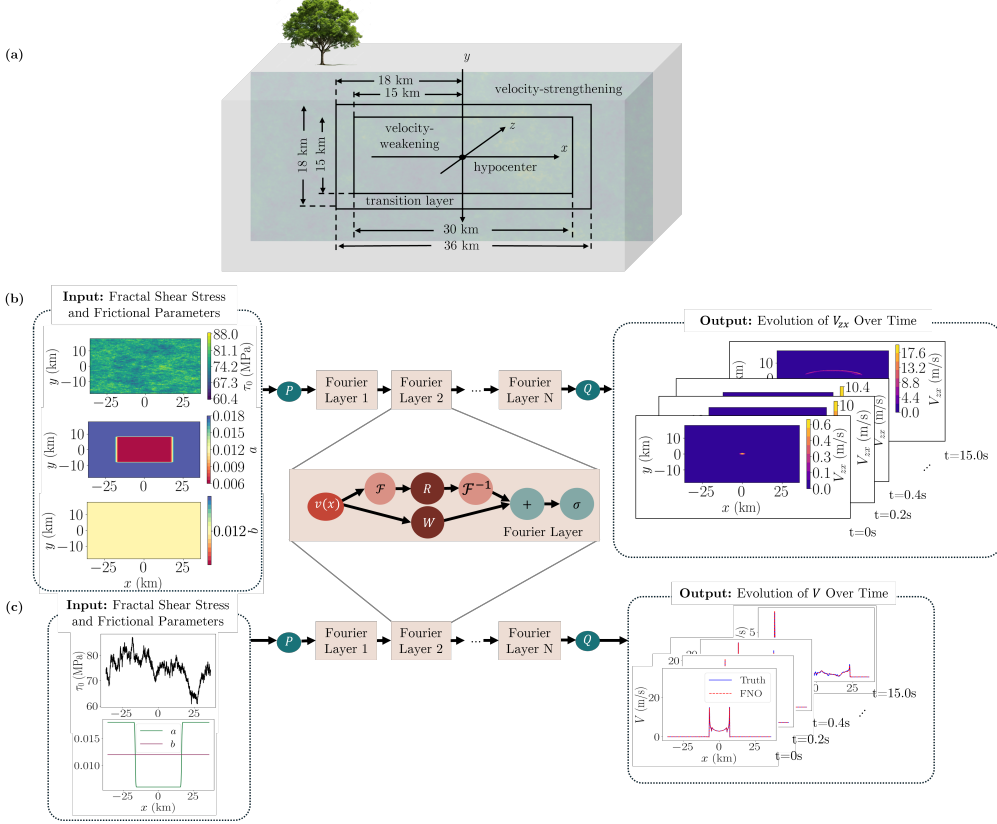


Figure 1. Schematic diagram of the proposed FNO framework. (a) Schematic illustration of the fault model, showing the central VW regime surrounded by the VS regime, with the hypocenter at the center. (b) FNO framework for a 2D fault plane embedded in a 3D bulk. (c) FNO framework for a 1D fault embedded in a 2D plane. The inputs include the distribution of initial shear stress and frictional parameters. The outputs are snapshots of slip rate over time.

$$\Delta a(x, y) = \Delta a_0 \left[1 - B(x; W, w) B \left(y; \frac{W}{2}, w \right) \right], \quad (11)$$

186

where the function $B(x; W, w)$ is defined as:

$$B(x; W, w) = \begin{cases} 1, & |x| \leq W, \\ \frac{1}{2} \left[1 + \tanh \left(\frac{w}{|x| - W - w} + \frac{w}{|x| - W} \right) \right], & W < |x| < W + w, \\ 0, & |x| \geq W + w. \end{cases} \quad (12)$$

187 We introduce variations into the initial shear stress field (τ_0) to capture spatial stress
 188 heterogeneity, which studies suggest follows a fractal-like distribution consistent with the
 189 roughness of fault surfaces (Andrews, 1980; Renard & Candela, 2017). Moreover, mod-
 190 els incorporating fractal distributions align with key seismological patterns, such as the
 191 Gutenberg-Richter law (Hirata, 1989). We generate a fractal shear stress field with a spec-
 192 ified fractal dimension D , mean, and standard deviation. The frequency-domain repre-
 193 sentation is constructed using a power-law scaling:

$$P(k) \propto \frac{1}{k^{2.5-D}}, \quad (13)$$

194 where k is the normalized wavenumber. This scaling yields larger amplitudes at
 195 low wavenumbers and smaller amplitudes at high wavenumbers.

196 We assign a random phase ϕ to each frequency component. The phase is drawn from
 197 a uniform distribution $\phi \sim \mathcal{U}(0, 2\pi)$. The complex frequency-domain representation is
 198 constructed as:

$$\text{Spectrum} = P(k) \cdot [\cos(\phi) + i \sin(\phi)], \quad (14)$$

199 After constructing the spectrum, we apply an inverse FFT to transform the data
 200 back into the spatial domain. The resulting real-valued shear stress field is normalized
 201 to ensure it matches the target statistical properties, including the specified mean and
 202 standard deviation:

$$S'(x) = \frac{S(x) - \mu}{\sigma} \cdot \sigma' + \mu', \quad (15)$$

203 where μ and σ are the mean and standard deviation of the raw field $S(x)$, and μ'
 204 and σ' are the mean and standard deviation of the scaled field $S'(x)$, respectively.

205 The fault's initial slip rate is prescribed as the constant $V_{ini} = 10^{-12}$ m/s. To sat-
 206 isfy the friction law, the initial state variable is computed for each spatial location, in-
 207 corporating the spatial variability of the parameter a and the imposed fractal shear stress
 208 distribution. The rupture is started by artificially overstressing a fault segment. Details
 209 of this nucleation procedure are provided in Appendix A.

210 2.3 Evaluating Model Predictions

211 The accuracy of predictions is assessed using a measure of the difference between
 212 the ground truth and the predicted slip rate over time. We present two error metrics:
 213 the relative L_2 error and the normalized root mean squared error (NRMSE). During the
 214 training and testing stages, the loss function is calculated using the relative L_2 error:

$$\text{Relative } L_2 \text{ error} = \frac{\|V_{pred}(\mathbf{x}, t) - V_{true}(\mathbf{x}, t)\|_2}{\|V_{true}(\mathbf{x}, t)\|_2} \quad (16)$$

215 where $V_{pred}(\mathbf{x}, t)$ is the predicted slip rate at location \mathbf{x} and time t , and $V_{true}(\mathbf{x}, t)$
 216 is the corresponding true value. However, this metric can be misleading sometimes be-
 217 cause the slip rate is close to zero at some points. As a result, the metric can be dispro-
 218portionately influenced.

219 Moreover, shifts in space and time are inherent in the dynamic rupture problem
 220 (Barall & Harris, 2015). These shifts introduce bias into the relative L_2 error calcula-
 221 tion, especially when the shifted prediction is compared to a small ground truth value.
 222 These biases will be discussed in each of the results sections. To address this issue, we
 223 introduce another metric, NRMSE:

$$\text{NRMSE} = \frac{\sqrt{\frac{1}{MN} \sum_{i=1}^M \sum_{j=1}^N \left(V_{pred,j}^{(i)} - V_{true,j}^{(i)} \right)^2}}{V_{max} - V_{min}} \quad (17)$$

Table 1. Parameters for the fault model

Medium Parameter	Symbol	Value
Shear wave speed (km/s)	c_s	3.464
Pressure wave speed (km/s)	c_p	6
Density (kg/m ³)	ρ	2670
Fault Parameters		
Reference coefficient of friction	f^*	0.6
Characteristic slip (m)	D_{RS}	0.02
Reference slip velocity (m/s)	V^*	10^{-6}
Length of VW patch in x direction (km)	$2W$	30
Width of VW patch in y direction (km)	W	15
Length of transition (km)	w	3
Length of the fault in x direction (km)	L_{fx}	72
Width of the fault in y direction (km)	L_{fy}	36
Evolution effect parameter	b	0.012
Steady state velocity dependence in VW patch	$a_{VW} - b$	varies
Steady state velocity dependence in VS patch	$a_{VS} - b$	varies
Initial velocity (m/s)	V_{ini}	10^{-12}
Initial normal stress (MPa)	σ_{ini}	120
Target mean of fractal shear stress (MPa)	μ'	75
Target standard deviation of fractal shear stress (MPa)	σ'	5
Nucleation Parameters		
Nucleation radius (km)	R	3
Maximum nucleation amplitude (MPa)	$\Delta\tau_0$	25
Final nucleation time (s)	T	1

where M is the total number of time steps, N is the total number of spatial points, $V_{pred,j}^{(i)}$ is the predicted value at spatial point j and time step i , and $V_{true,j}^{(i)}$ is the corresponding true value obtained from the numerical simulations. V_{max} and V_{min} are the maximum and minimum values of V_{true} over the entire space-time domain. NRMSE compares the error with the observed range of the ground truth. As such, the predictions will not be disproportionately influenced by small ground truth values.

3 Data Configuration

The dynamic rupture dataset is generated using the Spectral Boundary Integral (SBI) method, which is currently the fastest available solver for rupture propagation on a planar fault in a homogeneous medium (Geubelle & Rice, 1995; Kammer et al., 2021). The key parameters used in the model are summarized in Tables 1 and 2. The fractal dimensions are chosen to represent natural faults, with D varying between 1.2 and 1.6 (Renard & Candela, 2017). The rate-and-state frictional parameters fall within the observed range from laboratory experiments (Ikari et al., 2011). The dataset is obtained by solving the dynamic rupture problem over the time interval [0, 15] s.

Two datasets are generated, corresponding to 2D and 3D dynamic rupture simulations. The 3D simulation treats the fault as a 2D plane embedded in a 3D bulk, which is trained using FNO-2D, as shown in Figure 1b. It employs a 2D Fourier Transform to capture spatial correlations in both dimensions. The 2D simulation treats the fault as a 1D cross-section along the hypocenter in the x -axis. This dataset is trained using a sep-

244 arate FNO-1D, as shown in Figure 1c. It applies a 1D Fourier Transform to extract fre-
 245 quency features and efficiently learn spatial dependencies.

246 For the initial shear stress distribution, expressed in Equation 13, the normalized
 247 wave number k_i for the 1D fault is defined as:

$$k_i = \frac{i}{n_x} \quad (18)$$

248 where n_x is the total number of spatial points. We set $k_0 = 1$ for $i = 0$ to avoid
 249 division by zero. This choice is arbitrary as it only affects the mean value of the stress
 250 distribution which gets overridden later by matching the target mean value.

251 For the 2D fault, each grid point (i, j) in Fourier space corresponds to a wave num-
 252 ber pair (k_x, k_y) , defined as:

$$k_x = \frac{i}{n_x}, \quad k_y = \frac{j}{n_y}, \quad k = \sqrt{k_x^2 + k_y^2} \quad (19)$$

253 where n_x and n_y are the total number of points in the x and y directions, respec-
 254 tively.

255 3.1 2D Dynamic Rupture Dataset

256 In the 2D dataset, the fault is represented as a one-dimensional line embedded in
 257 a two-dimensional elastic bulk assuming plane strain conditions. A total of 4,000 real-
 258 izations are generated, with 1,000 realizations for each parameter set listed in Table 2.
 259 Of these, 3,600 realizations are allocated for training, while the remaining 400 realiza-
 260 tions are reserved for testing.

261 The FNO is trained to approximate the mapping from the initial shear stress and
 262 frictional parameters a and b to the sequence of slip rates over the time interval of inter-
 263 est. The input data is structured as a tensor of dimensions (N, X, C_{in}) , while the out-
 264 put data has dimensions (N, X, C_{out}) , where N denotes the number of realizations, X
 265 represents the number of spatial discretization points, C_{in} and C_{out} correspond to the
 266 number of input and output channels, respectively.

267 The spatial discretization consists of 2,880 points, i.e., $X = 2,880$, which corre-
 268 sponds to the discretization of the SBI solver. The input channels comprise the spatial
 269 distributions of initial shear stress, parameter a , and parameter b , resulting in $C_{\text{in}} = 3$.

270 We solve the system of equations using SBI with a time step Δt of 0.001 s to sat-
 271 isfy the Courant–Friedrichs–Lewy (CFL) condition, $\Delta t \leq f\Delta x/c_p$ with f is of order
 272 1. Here we take f equal to 0.25. Since FNOs are independent of discretization, we can
 273 use a coarser time step in FNO because we aim to perform a single-shot prediction up
 274 to 15 s, and a time step of 0.001 s poses significant memory challenges. As such, the out-
 275 put channels represent snapshots of the slip rate at discrete time steps of 0.2 s, spanning
 276 the duration from $t = 0$ s to $t = 15$ s, yielding 76 time steps and thus $C_{\text{out}} = 76$.

277 Before training, the dataset is normalized, scaling each feature in both the input
 278 and output to the range $[0, 1]$. After training, the original physical scale is restored us-
 279 ing an inverse transformation. This normalization enhances numerical stability and fa-
 280 cilitates efficient training of the FNO model (Cuomo et al., 2022).

Table 2. Fractal dimensions and variation of frictional parameter a and b for 2D and 3D dynamic rupture dataset

D	Δa_0	a_0	b
1.2	0.006	0.009	0.012
1.5	0.008	0.008	0.012
1.5	0.010	0.007	0.012
1.6	0.012	0.006	0.012

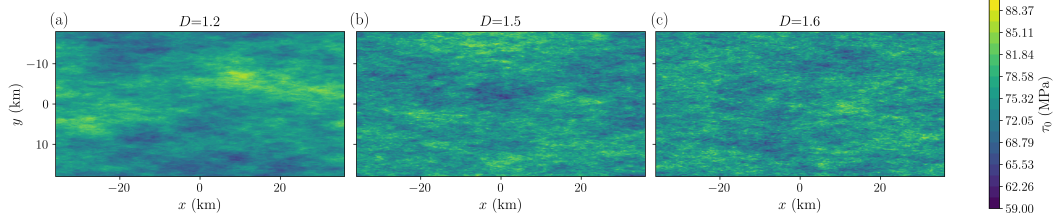


Figure 2. Initial fractal shear stress distributions τ_0 with fractal dimensions of (a) 1.2, (b) 1.5, and (c) 1.6. The target mean is set to 75 MPa, with a target standard deviation of 5 MPa.

281 3.2 3D Dynamic Rupture Dataset

282 In the 3D dataset, the fault is modeled as a two-dimensional plane embedded in
 283 a three-dimensional elastic bulk. A total of 4,000 realizations are generated, with 3,600
 284 realizations used for training and 400 realizations for testing. The variations in fractal
 285 dimension and frictional parameters a and b are listed in Table 2, with each parameter
 286 set containing 1,000 realizations. Examples of fractal initial shear stress distributions gen-
 287 erated using different fractal dimensions are illustrated in Figure 2.

288 As in the 2D case, the FNO is trained to approximate the mapping from the ini-
 289 tial shear stress and frictional parameters a and b to the sequence of slip rates over the
 290 time interval of interest. The input data is structured as a tensor of dimensions (N, X, Y, C_{in}) ,
 291 while the output data has dimensions $(N, X, Y, C_{\text{out}})$, where X and Y represent the num-
 292 ber of spatial discretization points in the x and y directions, respectively.

293 The two-dimensional fault is discretized into 720×360 spatial points, i.e., $X =$
 294 720 and $Y = 360$. The input channels consist of the spatial distributions of initial shear
 295 stress, parameter a , and parameter b , resulting in $C_{\text{in}} = 3$.

296 It is worth noting that the time step Δt in the SBI solver is 0.01 s to satisfy the
 297 CFL condition with $\Delta x = \Delta y = 100$ m and $f = 0.6$. We output the SBI solution at
 298 a frequency of 0.1 s. The discretization consists of 720×360 spatial points. This results
 299 in $(N, X, Y, C_{\text{out}}) = (3600, 720, 360, 150)$, producing approximately 500 GB of data. Given
 300 the available memory and GPU limitations, training with a single batch at this scale is
 301 challenging. To address this, we reduce the number of spatial and temporal points by
 302 sub-sampling from $(X, Y, C_{\text{out}}) = (720, 360, 150)$ to $(360, 180, 76)$ for FNO training, re-
 303 ducing the dataset size to approximately 66 GB. In this case, the output channels cor-
 304 respond to snapshots of slip rate spatially sampled at half the resolution of the original
 305 simulations and temporally recorded at 0.2 s intervals, covering the time range $t = 0$
 306 s to $t = 15$ s, thus $C_{\text{out}} = 76$. This adjustment makes training feasible on the avail-
 307 able NVIDIA A100 GPU with 64 GB of memory.

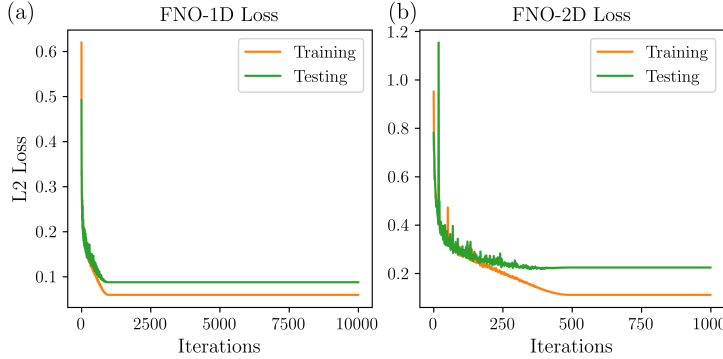


Figure 3. Training and testing losses for (a) 2D dynamic rupture dataset and (b) 3D dynamic rupture dataset.

As with the 2D dataset, we also normalize the 3D dataset, scaling each feature in both the input and output to the range [0, 1]. After training, the original physical scale is restored using an inverse transformation.

4 Results

4.1 FNO-1D for 2D Dynamic Rupture Dataset

4.1.1 Training and Testing Performance

We optimize the hyperparameters of FNO-1D, including the number of modes, Fourier layers, lifting and projection layers, and the learning rate. Details of hyperparameter tuning and training strategies are listed in Appendix B. The model selection criterion balances accuracy with computational efficiency by maintaining a minimal number of parameters. Based on this tuning process, we configure the model with four Fourier layers ($m = 4$), while the lifting network P and projection network Q each consist of 128 neurons. The number of retained modes after applying the Fourier transform and subsequent linear transformation is set to 16. The activation function employed is the Gaussian Error Linear Unit (GELU) (Hendrycks & Gimpel, 2016). The model is trained using a batch size of 10, with a relative L_2 loss function and the Adam optimizer (Kingma & Ba, 2014), adopting a learning rate of 10^{-3} and a weight decay of 10^{-4} with a cosine annealing schedule. The training process is conducted for 10,000 epochs. The training and testing losses are shown in Figure 3. Both training and testing losses consistently decrease without significant divergence between them, indicating no signs of overfitting. Some fluctuations in the testing loss at the beginning occur due to the selected batch size.

The performance of FNO-1D is evaluated on the testing dataset. The model predictions, compared against the ground truth, are presented in Figure 4. FNO-1D effectively captures a wide range of magnitudes arising from different distributions of τ_0 and the frictional parameters a and b . The model successfully reproduces the global slip rate, particularly in regions characterized by sharp gradients, such as the rupture front. Discrepancies arise in regions where resolving closely spaced high-frequency components is required. These features reflect a phenomenon known as spectral bias (Rahaman et al., 2019; Cao et al., 2019; Kong et al., 2025), which implies that deep learning models predict high-frequency features less accurately than lower-frequency ones. In Appendix B, we discuss a potential strategy for improving the model's performance at higher frequencies by implementing a specialized training protocol.

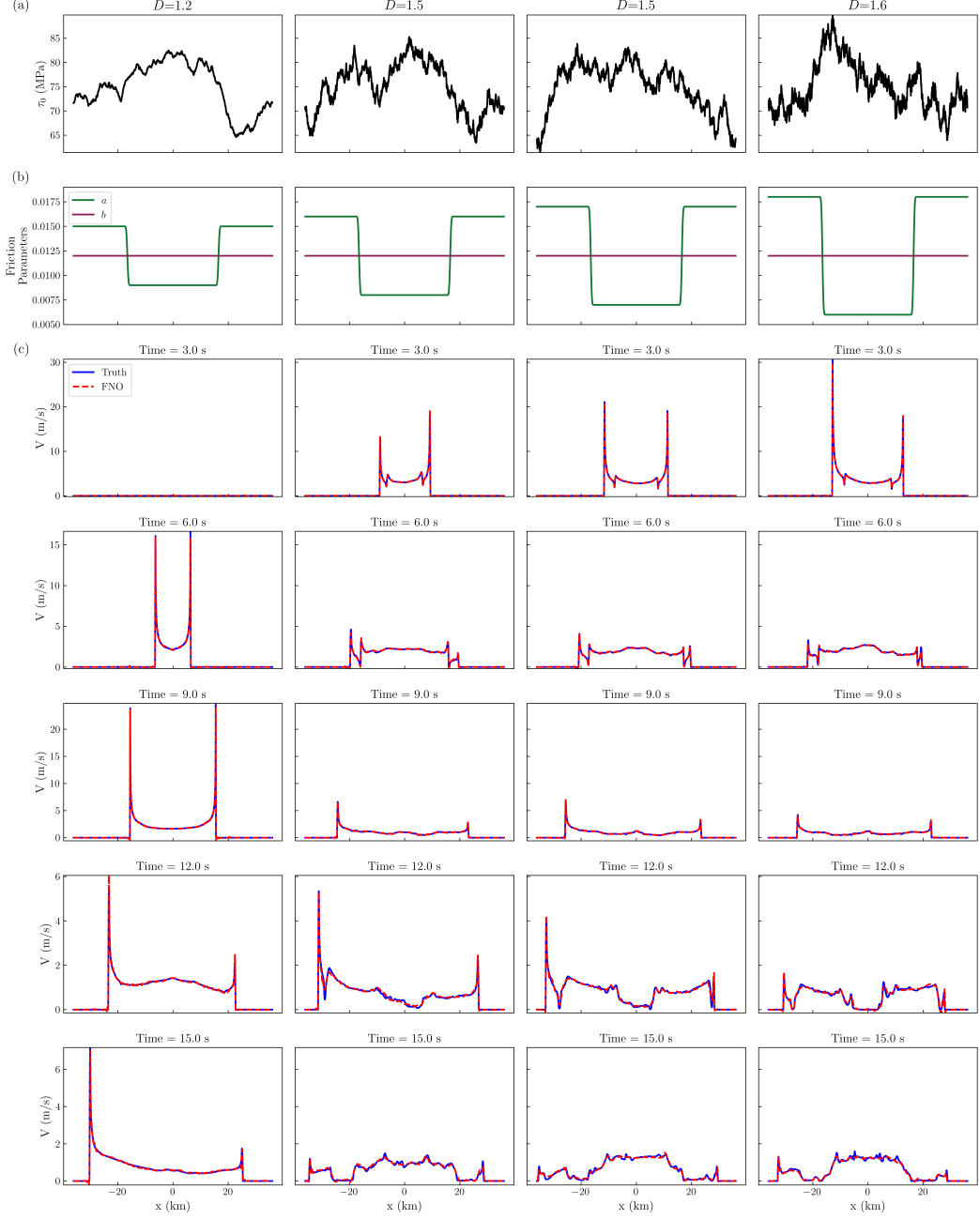


Figure 4. Testing of the trained FNO-1D model on the 2D dynamic rupture test dataset: (a) Inputs include initial fractal shear stress distributions τ_0 and (b) frictional parameters a and b ; (c) Outputs consist of predicted slip rate snapshots at selected discrete time steps.

Table 3. Median and median absolute deviation (MAD) of NRMSE and relative L_2 error in the bracket shown in Figure 5 for 3600 training samples and 400 testing samples of 2D and 3D dynamic rupture datasets.

	2D Dynamic Rupture	3D Dynamic Rupture
	NRMSE (Relative L_2 Error)	NRMSE (Relative L_2 Error)
Training	0.00261 ± 0.000477 (0.0550 ± 0.00966)	0.00231 ± 0.000377 (0.0854 ± 0.0129)
Testing	0.00329 ± 0.000852 (0.0685 ± 0.0209)	0.00387 ± 0.00132 (0.153 ± 0.0514)

We summarize the NRMSE and relative L_2 error on the training and testing datasets in Figure 5. Testing samples show slightly higher errors but still follow the same distribution as the training set, suggesting no major overfitting. The majority of samples have small errors and are highly skewed towards zero, with the median and median absolute deviation (MAD) of the errors presented in Table 3. According to Figure 5b, more than 90% of the training set shows a relative L_2 error of less than 10%, while this fraction drops to 80% for the testing set. Examples of the predictions corresponding to different selected values of the relative L_2 error are presented in the supplementary information.

4.1.2 Generalization to Unseen Initial Shear Stress

An advantage of FNOs is that they can target the underlying operator, and learn to handle a family of problems rather than a single instance. Accordingly, in this section we test the generalization of our trained operator to some unseen initial conditions.

We evaluate the trained FNO-1D model, originally trained on initial fractal shear stress τ_0 , using a uniform initial shear stress consistent with TPV101 problem description (Harris et al., 2018, 2009; Kammer et al., 2021). The initial shear stress of $\tau_0 = 75$ MPa is prescribed along the entire fault. This value is within the range of shear stress values in the fractal dataset. However, the network has not seen a spatially uniform case before this test. We compare predictions from the FNO-1D model against the ground truth in Figure 6. The computed NRMSE and relative L_2 error between the predictions and ground truth are 0.00963 and 0.1822, respectively. FNO-1D shows ability to capture slip rate evolution, particularly during rupture propagation in the VW regime and transitioning into the VS region. We observe noise, spatial shifts in the predictions, and slight mismatches in peak magnitudes at later times. Such discrepancies contribute to the high relative L_2 error. However, the global features of slip rate remains consistent with the ground truth. These results highlight the robustness of FNO-1D, as the model successfully generalizes to this unseen distribution of τ_0 .

Additionally, we test the performance of FNO-1D on an unseen fractal dimension D . Specifically, we evaluate the trained model using a dataset generated with $D = 1.3$, which was not part of the training set. In this case, the frictional parameter a follows a boxcar distribution, with $a = 0.008$ in the VW region and $a = 0.016$ in the VS region, while the frictional parameter b is fixed at 0.012. Figure 7 shows the results from FNO-1D compared to the ground truth, with NRMSE and relative L_2 error of 0.00353 and 0.0566, respectively. FNO-1D effectively captures both the low-frequency and high-frequency components of the slip rate up to approximately 12 s. The magnitude of the rupture front in the predictions also aligns with the ground truth. Some discrepancies occur when predicting the high-frequency component at later times. This test further

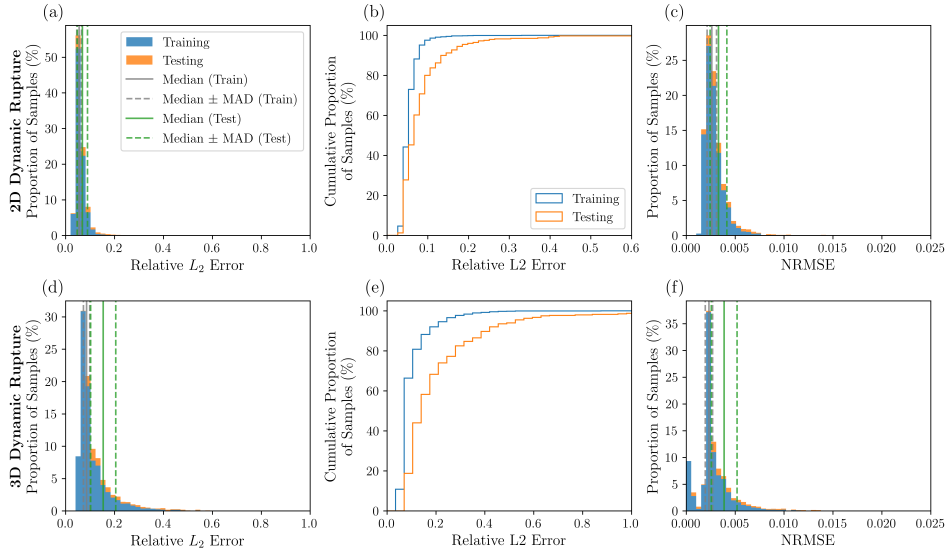


Figure 5. Error analysis for 2D and 3D dynamic rupture predictions. (a) and (d) show histograms of the relative L_2 error distributions for the training (blue) and testing (orange) datasets in the 2D and 3D cases, respectively. Similarly, (c) and (f) show histograms of the NRMSE distributions for the training (blue) and testing (orange) datasets in the 2D and 3D cases. The vertical lines indicate the median error for the training (gray solid) and testing (green solid) datasets, as well as the median \pm median absolute deviation (MAD) range for the training (gray dashed) and testing (green dashed) datasets. (b) and (e) show the cumulative histograms of the relative L_2 error distributions for the training (blue) and testing (orange) datasets in the 2D and 3D cases, respectively.

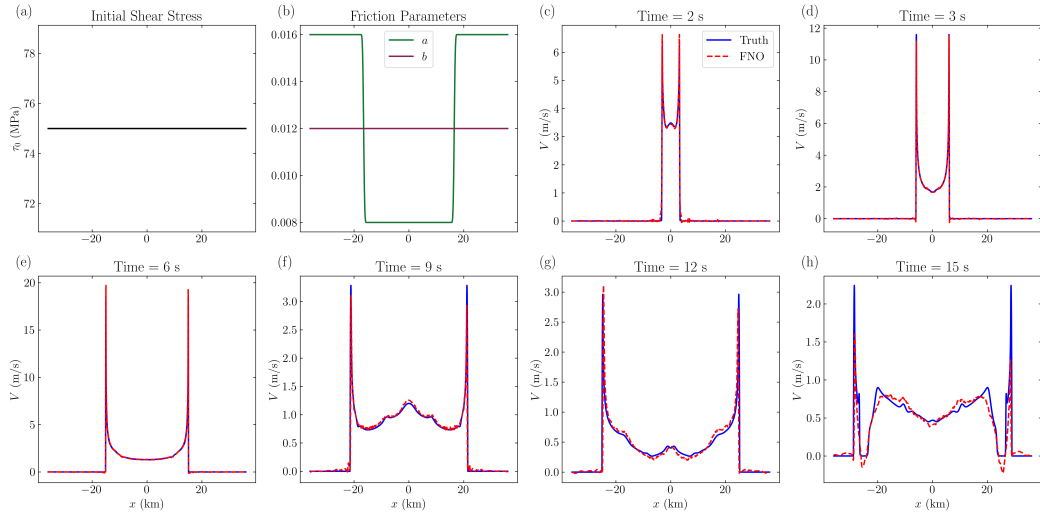


Figure 6. Results of FNO-1D testing on an unseen shear stress distribution from the TPV101 SCEC/USGS benchmark: (a) Inputs include a uniform initial shear stress (τ_0) of 75 MPa and frictional parameters a and b , with $\Delta a_0 = 0.008$ and $a_0 = 0.008$; (b) Outputs consist of predicted slip rate profiles at selected time steps.

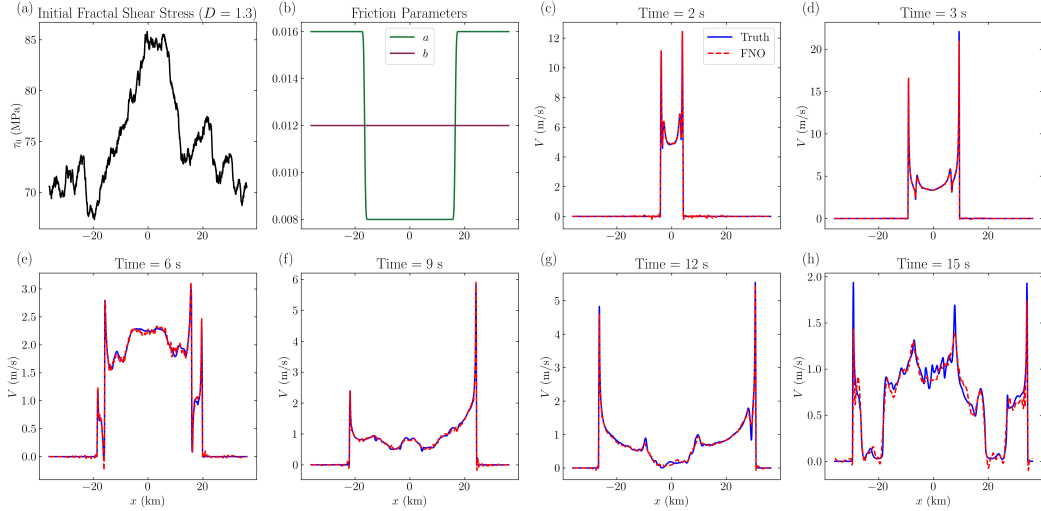


Figure 7. Results of FNO-1D testing on an unseen fractal dimension $D = 1.3$: Inputs consist of (a) initial fractal shear stress distributions (τ_0) with $D = 1.3$ and (b) frictional parameters a and b , with $\Delta a_0 = 0.008$ and $a_0 = 0.008$; (c) - (h) Outputs consist of predicted slip rate profiles at selected time steps.

corroborates the potential of FNO-1D in predicting slip rates under unseen initial shear stress conditions.

4.1.3 Generalization to Unseen Frictional Parameters

We test the FNO-1D model on unseen frictional parameters, specifically parameter a , with values of 0.0075 in the VW region and 0.0165 in the VS region, while parameter b is set uniformly to 0.012 along the fault. The initial shear stress τ_0 follows a fractal distribution with fractal dimension $D = 1.5$. Figure 8 compares the predicted slip rates with the ground truth, showing NRMSE and relative L_2 error of 0.0213 and 0.4290, respectively. FNO-1D captures the overall evolution trend, although some discrepancies occur at the peaks of the rupture front in the beginning. The high relative L_2 error results from mismatches in the magnitude between predictions and ground truth at the start, as well as spatial shifts occurring around 9 s. Additionally, the slip rates at the initial time step have a very small magnitude close to zero, which amplifies the relative L_2 error value without indicating significant mismatches. Despite these issues, FNO-1D predicts, reasonably well, the major features of the slip rate evolution under this unseen frictional conditions.

4.2 FNO-2D for 3D Dynamic Rupture Dataset

4.2.1 Training and Testing Performance

We perform hyperparameter tuning for FNO-2D, resulting in an architecture consisting of four Fourier layers. The lifting and projecting fully connected neural networks each contain 128 neurons. After applying the Fourier transform, 32 modes are retained in the linear transformation, and the GELU activation function is employed. The model is trained using the Adam optimizer with a batch size of 10, a learning rate of 10^{-3} , and a weight decay of 10^{-4} , following a cosine annealing schedule. Training spans 1,000 epochs until the loss stabilizes. Training and testing losses over optimization iterations are shown

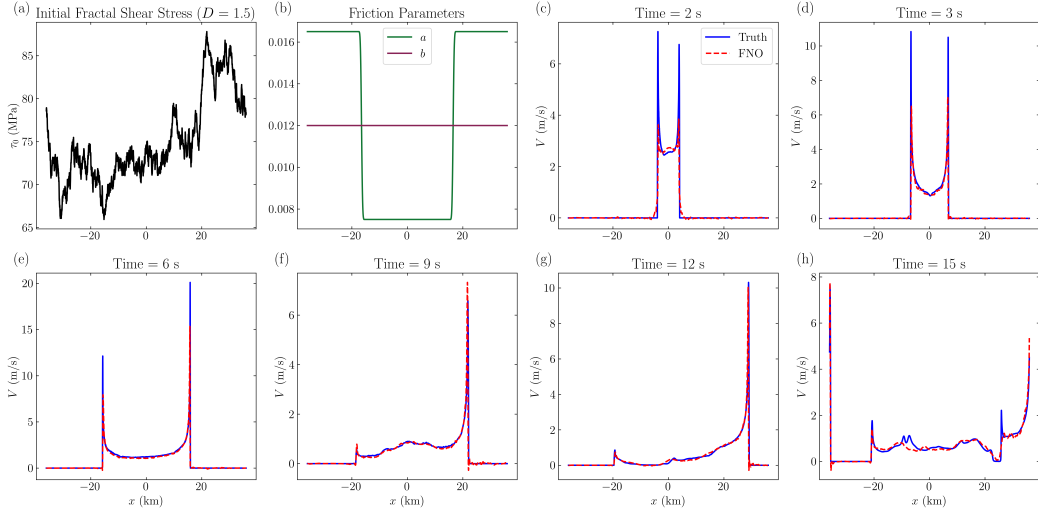


Figure 8. Results of FNO-1D testing on unseen $a - b$: Inputs consist of (a) τ_0 with $D = 1.5$, along with (b) frictional parameters a and b , with $\Delta a_0 = 0.009$ and $a_0 = 0.0075$; (c) - (h) Outputs consist of predicted slip rate profiles at selected discrete time steps.

in Figure 3b. Both training and testing losses consistently decrease without significant divergence, indicating no signs of overfitting.

Figure 9 illustrates a successful example of the predictions compared to the ground truth. It shows the rupture front contours in the VW region at 5-second intervals, along with time series at six selected points in the VW region. FNO-2D accurately captures the spatially irregular shape of the rupture front contours with NRMSE of 0.00636 and relative L_2 error of 0.2448. The model's accuracy is high during the initial nucleation phase but decreases over time due to minor shifts in the rupture front arrival times. This loss in accuracy over time is also pointed out in time-series prediction (Zhang et al., 2023). Nonetheless, the time histories at randomly selected points still exhibit good overall agreement. The minor time shifts observed during the later part of the rupture propagation amplifies the relative L_2 error. However, the overall agreement between the model prediction and the ground truth remains high.

The distribution of relative L_2 error and NRMSE during the prediction phase, shown in Figure 5, further confirms that no overfitting is occurring, as the testing dataset follows the same trend as the training dataset. Moreover, the distribution is skewed toward zero. More than 80% of the training dataset has relative L_2 errors less than 20%, while this proportion drops to 60% for the testing dataset. Interestingly, we have found that even in cases where the model predictions show higher relative L_2 errors, the model still successfully captures the major features of rupture dynamics. Examples of predictions with higher relative error are provided in the supplementary information.

4.2.2 Generalization to Unseen Initial Shear Stress

We evaluate the trained FNO-2D model using an unseen initial shear stress distribution, specifically, the uniform stress distribution defined in the TPV101 benchmark from the SCEC/USGS dynamic earthquake rupture code verification exercise. In this benchmark, the initial shear stress is uniformly set to 75 MPa, while frictional parameters remain within the training range of the 3D dynamic rupture dataset. Figure 10 shows the rupture contours of the predicted component of slip rate V_{zx} compared to the ground

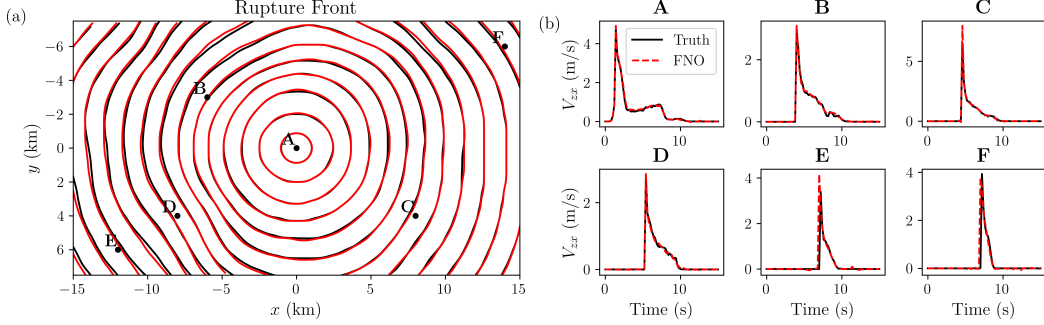


Figure 9. Results of FNO-2D on the testing dataset for 3D dynamic rupture. The inputs include the initial fractal shear stress with $D = 1.5$ and frictional parameters: a with $\Delta a_0 = 0.008$ and $a_0 = 0.008$, and $b = 0.012$, over the spatial domain. (a) Rupture front contour plot, showing progression at 0.5 s intervals. (b) Time histories of slip rate at selected points in the VW region.

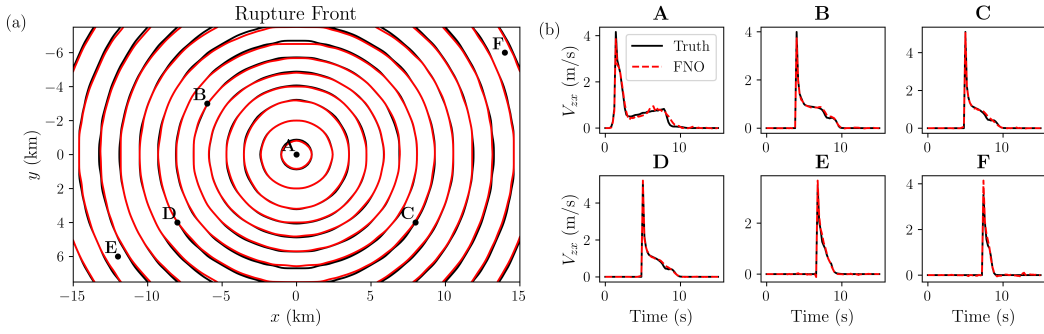


Figure 10. Results of FNO-2D testing on an unseen shear stress distribution from the TPV101 SCEC/USGS benchmark with a uniform shear stress of 75 MPa, $\Delta a_0 = 0.008$, $a_0 = 0.008$, and $b = 0.012$. (a) Rupture front contour plot of the ground truth (black) and predictions (red), showing progression at 0.5 s intervals. (b) Time histories of slip rate at selected points in the VW region.

truth, as well as the time history at six selected points in the VW region. FNO-2D can capture the evolution of V_{zx} . The predicted rupture front aligns closely with the ground truth with NRMSE of 0.0100 and relative L_2 error of 0.2867. The predicted time series also match well with the ground truth, capturing the peaks and fine-scale details of V_{zx} over time. The errors in the magnitude of peaks are less than 1%, with some noise observed during the period between the first and second drops at point A. The accuracy drops for points located closer to the VW domain boundaries, with some minor shifts in arrival times and slightly larger mismatch in the peaks (e.g., points E and F). However, overall, there is good agreement between the model predictions and the ground truth. This demonstrates the potential of FNO-2D in capturing the highly nonlinear evolution of slip rate over time, even under an initial shear stress distribution not previously seen during training.

Additionally, we test the model on a fractal initial shear stress distribution with an unseen fractal dimension $D = 1.3$, similar to the FNO-1D case. The frictional parameters are identical to those used previously with FNO-1D. The predictions, presented in terms of the rupture front and time series at selected points in Figure 11, show agreement with the ground truth. The shape of the predicted rupture front aligns with the

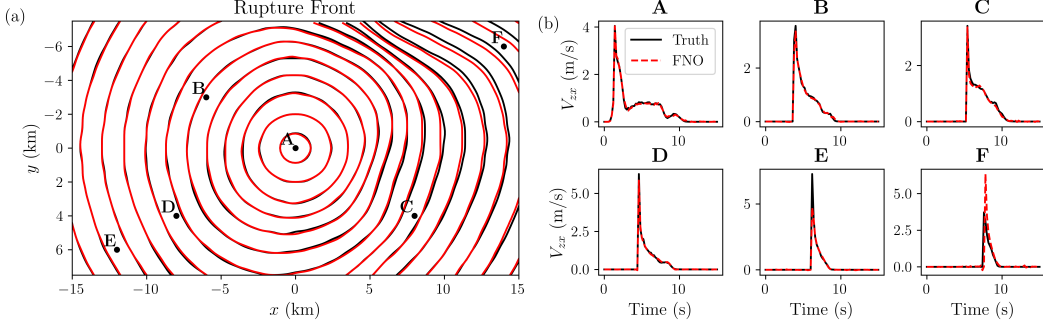


Figure 11. Results of FNO-2D testing on an unseen fractal dimension $D = 1.3$ of the initial fractal shear stress. The frictional parameters are $\Delta a_0 = 0.008$, $a_0 = 0.008$, and $b = 0.012$: (a) Rupture front contour plot of the ground truth (black) and predictions (red), showing progression at 0.5 s intervals. (b) Time histories of slip rate at selected points in the VW region.

ground truth initially, though the match slightly decreases over time, resulting in a NRMSE of 0.00906 and a relative L_2 error of 0.3883 for this realization. We note that shifts in the rupture front can cause a high relative L_2 error despite the visual agreement. This is due to the small ground truth values, close to zero, being compared to the peak slip rates in the shifted rupture front. The time series at point E shows slight differences in the peak slip rate. However, it still captures the overall trend of the evolution. This demonstrates that FNO-2D generalizes effectively to different fractal dimensions of τ_0 .

4.2.3 Generalization to Unseen Frictional Parameters

We evaluate the generalization performance of the trained FNO-2D model on previously unseen frictional parameter values. Specifically, parameter a is set to 0.0075 in the VW region and 0.0165 in the VS region, while parameter b is uniformly fixed at 0.012 along the fault. The initial shear stress τ_0 is modeled using a fractal distribution with fractal dimension $D = 1.5$. Figure 12 presents a successful case of the predicted rupture front and corresponding time series of V_{zx} at selected spatial locations. We observe spatial shifts in the rupture front contours, which amplify the NMRSE and relative L_2 error to 0.0171 and 0.6051, respectively. Some mismatches at the peaks of V_{zx} over time at selected points also contribute to this error. While the FNO-2D still captures the global features of the temporal evolution of V_{zx} across nucleation, propagation, and arrest phases, we later discuss specific challenges related to generalizing to unseen frictional properties and how to possibly improve the relative L_2 error.

4.3 Computational Efficiency Analysis

We summarize the computational efficiency of FNO-1D and FNO-2D in Table 4. The training and testing times are both evaluated on an Nvidia A100 GPU. Once the models are trained, they can be directly used as an alternative to numerical simulators.

For the application we are proposing, the trained model is used directly for subsequent predictions. Therefore, we compare the FNO model's performance to the computational time required by a numerical solver. To evaluate the computational speed-up, we compare the numerical simulation run time on an AMD EPYC 7763 "Milan" (PCIe Gen4) CPU to the FNO's testing time. The run times are 345 s for the 2D simulation and 1182 s for the 3D simulation. The predictions from the 2D and 3D simulations are

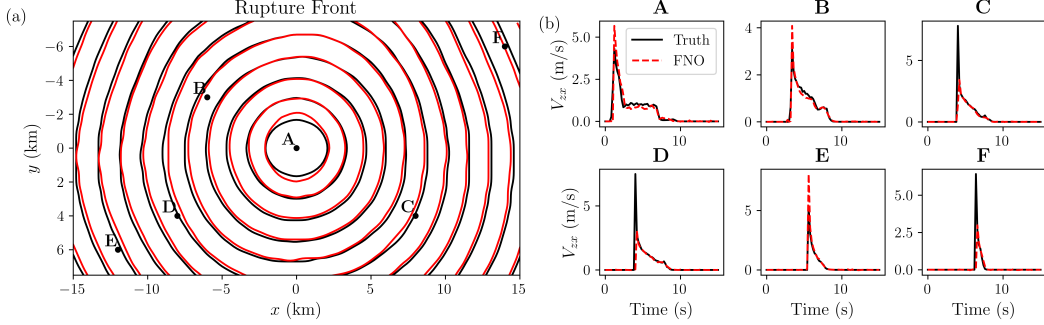


Figure 12. Results of FNO-2D testing on an unseen $a - b$ distribution. Inputs consist of frictional parameters a and b , with $\Delta a_0 = 0.009$, $a_0 = 0.0075$, and $b = 0.012$, along with an initial shear stress distribution τ_0 with a fractal dimension $D = 1.5$. (a) Rupture front contour plot showing progression at 0.5 s intervals. (b) Time histories of slip rate at selected points in the VW region.

Table 4. Comparison of different models in terms of parameters, training time, testing performance, and speed-up. The testing times are calculated by taking the median of 100 random cases. The speed-up is compared with numerical simulation run time of 345 s for 2D and 1182 s for 3D.

# Parameter	Training (-)	Testing	
		Prediction time (s)	Speed-up vs. numerical simulation (times)
FNO-1D	2,348,492	3	2×10^5
FNO-2D	268,739,404	130	4×10^5

2 $\times 10^5$ and 4×10^5 times faster than the conventional numerical simulation, respectively.

Notably, the prediction time does not increase significantly, despite the substantial increase in the number of parameters, from 2D to 3D. The training time is slower for the 3D simulation. However, we prioritize prediction accuracy and testing time over the off-line training time.

5 Discussion and Conclusion

To overcome the computational bottleneck of classical physics-based earthquake models, we present an FNO-based surrogate model to accelerate dynamic rupture simulations. In the surrogate model, we predict the evolution of the slip rate distribution on the fault plane, given the initial distribution of shear stress and frictional parameters a and b in the rate-and-state friction law, a commonly used friction law in earthquake modeling. The ground truth is generated using the SBI method with different fractal shear stress and frictional parameter distributions in both 2D and 3D homogeneous domains. Each dataset is trained and tuned separately using FNO-1D and FNO-2D. We select the hyperparameters based on a balance between computational efficiency and accuracy as discussed in Appendix B. As a result, we achieve speedups of 4×10^5 and 2×10^5 compared to the SBI method in 3D and 2D dynamic rupture problems, respectively. This increase in speed potentially enables more efficient dynamic rupture inversion, statistical analysis, and identification of extreme events in ensembles of earthquake rupture forecasts.

498 Predicted slip rates are evaluated using pointwise metrics, including the normal-
499 ized root mean squared error (NRMSE), which compares predictions with the observed
500 range of the ground truth, and the relative L_2 error, which assesses the discrepancy at
501 discrete points in the domain. We demonstrate that the training process of FNO-based
502 models does not exhibit overfitting. Test set predictions show strong agreement with the
503 ground truth. Specifically, for the 2D dynamic rupture dataset, the median NRMSE is
504 0.329% and the median relative L_2 error is 6.85%. For the 3D dynamic rupture dataset,
505 the median NRMSE is 0.387% and the median relative L_2 error is 15.3%.

506 Higher errors in the 3D problem are primarily due to down-sampling to a lower res-
507 olution than the physical problem, resulting in a grid size that may smear some details
508 in the process zone region. This limitation is due to constrained computational resources.
509 Access to additional resources would allow training at higher resolution, potentially re-
510 ducing these errors to a level comparable to what is seen in the 2D problem. The errors
511 are generally more pronounced in regions with high-frequency features, reflecting the spec-
512 tral bias, which states that deep learning models tend to favor low-frequency components.
513 To further improve model performance, we suggest training on a specialized dataset, with
514 the most critical hyperparameter being the width of P and Q . This opens opportuni-
515 ties for further improving the model performance by increasing the size of the training
516 dataset as well as increasing the model complexity.

517 Furthermore, we test the model under unseen initial stress distributions and fric-
518 tional parameters. The FNO-based models demonstrate robustness when applied to out-
519 of-distribution cases, such as a uniform initial stress distribution. Under this distribu-
520 tion, the problem setup corresponds to the SCEC/USGS verification exercise. Addition-
521 ally, we evaluate the model on an initial shear stress distribution with an unseen frac-
522 tal dimension of $D = 1.3$. The FNO-based models maintain good accuracy under these
523 conditions, with NRMSE values lower than 1%. We also test FNO-1D and FNO-2D on
524 unseen frictional parameters. While we have demonstrated successful predictions for un-
525 seen frictional parameters, the model's performance is less robust compared to tests in-
526 volving unseen shear stress. This reduced robustness may be attributed to the fact that
527 variations in frictional parameters modify the underlying material model and consequently
528 change the properties of the governing operator. In contrast, changing the shear stress
529 distribution affects only the initial conditions without modifying the governing equations.
530 This limitation could potentially be addressed by incorporating a greater variety of fric-
531 tional parameters during training. One important source of error in FNO predictions is
532 spatial and temporal shifts. When the slip rate is small, the relative L_2 error can be am-
533 plified, particularly where sharp, high-value rupture fronts shift in space and time rel-
534 ative to small slip rate values.

535 We highlight a couple of key aspects of FNO as applied to our problem. The FNO
536 neural approximation effectively captures the evolution of slip rate over extended peri-
537 ods. The FNO formulation is time-continuous and can be discretized as needed for train-
538 ing and application. Furthermore, the FNO enables the use of data generated at vary-
539 ing spatial and temporal discretizations. Traditional solvers must adhere to stability con-
540 dition to maintain stability, whereas this constraint does not apply to FNOs, allowing
541 for greater flexibility in discretization and time stepping. Third, the FNO shows poten-
542 tial for successful generalization to unseen stress and frictional condition although our
543 findings suggest that the performance will further improve by training on larger data sets.

544 We conclude with a discussion of limitations and potential future directions. First,
545 this work assumes a specific mean and standard deviation for the input distributions.
546 Future work should explore training the FNO on datasets with more diverse parameter
547 distributions. Second, the current FNO is trained on datasets generated using a specific
548 nucleation protocol. To improve generalization, training the model on a broader range
549 of nucleation parameters, including variation in the nucleation site, is desirable. Third,
550 the FNO is trained for predictions within a fixed time interval. Extending the predic-

tion horizon beyond a specific interval could involve recursive training, enabling the model to predict slip evolution iteratively. Furthermore, a hybrid approach combining traditional numerical solvers with FNOs could enable long-range predictions. A key aspect of this approach would be defining a robust criterion, such as a physics-guided error threshold, for switching between FNO and traditional solvers. Finally, access to larger training datasets and more GPUs will further imporve the performance of FNOs and their ability to generalize. A community effort for creating a database for dynamic rupture simulations would be beneficial in that respect.

Appendix A Details on Model Setup

Rupture is nucleated by applying a time- and space-dependent perturbation to the horizontal shear traction. The perturbation grows smoothly from zero to its maximum amplitude $\Delta\tau_0$ over a finite time interval (T) and is confined to a circular region of radius (R) centered on the hypocenter. The nucleation perturbation is expressed as:

$$\Delta\tau(x, t) = \Delta\tau_0 F(x - x_0) G(t), \quad (\text{A1})$$

where the spatial function $F(r)$ and temporal function $G(t)$ are given by:

$$F(r) = \begin{cases} \exp\left(\frac{r^2}{r^2 - R^2}\right), & r < R, \\ 0, & r \geq R, \end{cases} \quad (\text{A2})$$

$$G(t) = \begin{cases} \exp\left[\frac{(t-T)^2}{t(t-2T)}\right], & 0 < t < T, \\ 1, & t \geq T. \end{cases} \quad (\text{A3})$$

Appendix B FNO Hyperparameters Tuning and Training Strategies

This section presents the training strategies and the influence of hyperparameters on prediction accuracy. For the 2D dynamic rupture dataset, we tune the model by varying the number of Fourier modes, the number of Fourier blocks, and the learning rate over 50 epochs. The number of retained Fourier modes is initially selected as 16 and 32, while the number of Fourier layers is set to 4, 5, and 6. The depth of the fully connected layers P and Q is chosen from 32, 64, 128, and 256. We consider two learning rates, 0.001 and 0.0005, while fixing the batch size at 10. Based on Table B1, we find that models with four Fourier layers generally yield the lowest error, with the best-performing candidates highlighted in bold. These candidates are selected based on a balance between the total number of parameters in the FNO model and prediction accuracy. We further train these models for 500 epochs, and the differences in relative L_2 error among the top three models remain insignificant, specifically within a 1% difference. Consequently, we select the final model as the one with the lowest number of parameters, consisting of four Fourier layers, 32 Fourier modes, a width of 128 for the lifting and projection layers, and a learning rate of 0.001. This model is then further trained for up to 10,000 epochs until the training and testing losses saturate. This approach helps save computational resources and allows for more efficient hyperparameter selection, especially for large datasets such as the 3D dynamic rupture dataset.

To improve accuracy, we propose training exclusively on a specific dataset with a chosen fractal dimension and frictional parameters. Here, we select a dataset with $D = 1.6$, $\Delta a_0 = 0.012$, and $a_0 = 0.006$ resulting in a training set of 900 realizations and a testing set of 100 realizations. We primarily tune the number of Fourier modes, the width of the lifting and projection layers, and the learning rate. The relative L_2 error for the

Table B1. Relative L_2 errors for different hyperparameter configurations, including the number of Fourier layers, modes, learning rate, and the widths of P and Q , on the 2D dynamic rupture testing dataset.

Fourier Layers	Learning Rate	Modes	Width of P and Q			
			32	64	128	256
4	0.001	16	0.327423	0.279825	0.199039	0.225360
		32	0.319402	0.263659	0.205039	0.206671
	0.0005	16	0.376180	0.306192	0.241678	0.214775
		32	0.361853	0.271715	0.238622	0.198188
5	0.001	16	0.324249	0.338498	0.328546	0.323920
		32	0.309520	0.340786	0.324978	0.321918
	0.0005	16	0.379091	0.340786	0.316518	0.312066
		32	0.352530	0.329741	0.322074	0.305138
6	0.001	16	0.330633	0.334641	0.324744	0.328914
		32	0.297148	0.343834	0.320379	0.321232
	0.0005	16	0.359399	0.275518	0.237807	0.425277
		32	0.328937	0.250830	0.273538	0.212822

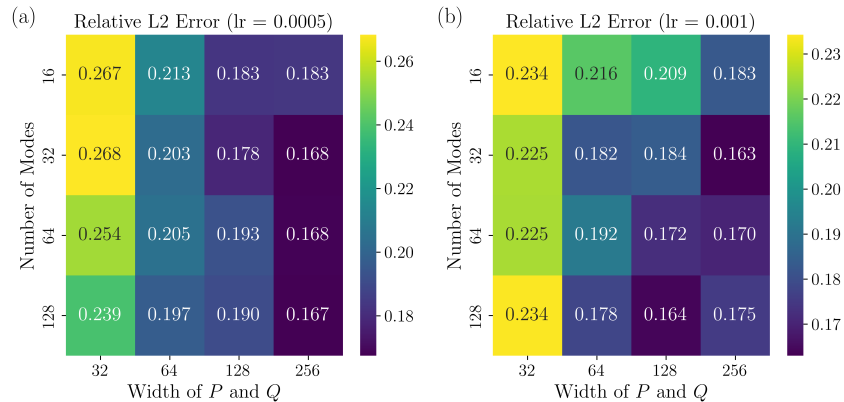


Figure B1. Heat map showing the relative L_2 error of 100 testing sets with inputs of fractal stress distribution at $D = 1.6$ and frictional parameters $\Delta a_0 = 0.012$ and $a_0 = 0.006$. The number of modes and the widths of P and Q are shown on the vertical and horizontal axes, respectively, with (a) a learning rate of 0.0005 and (b) a learning rate of 0.001.

testing set is shown in Figure B1. The number of modes is increased to 16, 32, 64, 128. We observe a decrease in error when increasing the depth of the fully connected layers P and Q . The most influential hyperparameter is the width when using a learning rate of 0.001. It is evident that the relative L_2 error decreases as the widths of P and Q increase, as indicated by the blue gradient on the right side of the heat map. Other hyperparameters, including the number of Fourier layers, the number of retained Fourier modes, and the learning rate, do not exhibit a clear pattern, and the error fluctuates.

After hyperparameter tuning, the revised model demonstrates enhanced predictive accuracy, with the predicted slip rates illustrated in Figure B2. In the zoomed inset of panel (f), the specialized FNO captures some high-frequency components better than the original FNO at $x \approx -10$ and $x \approx 10$ km. This improvement paves the way for further increasing the complexity of the FNO in future work.

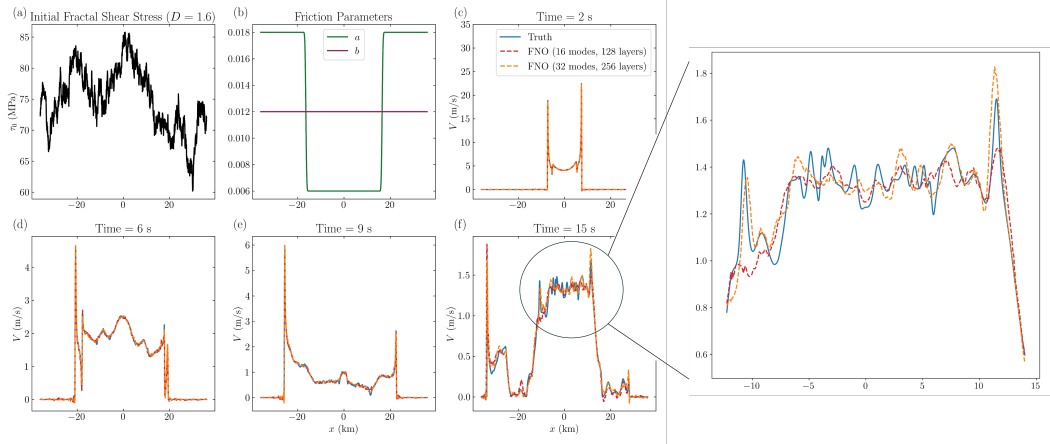


Figure B2. Results from FNO-1D (dashed red) are compared with those from the specialized FNO (dashed orange), which is trained on 900 separate sets of fractal stress distributions with $D = 1.6$ and frictional parameters a and b (with $\Delta a_0 = 0.012$ and $a_0 = 0.006$; dashed orange) and with the ground truth (solid blue). (a) and (b) show the inputs, including the initial shear stress and frictional parameters, while (c) - (f) are the outputs, consisting of predicted slip rate snapshots at selected discrete time steps.

For the 3D dynamic rupture dataset, we primarily tune the model while keeping the number of Fourier layers fixed at four, based on insights from the 2D dynamic rupture dataset. The number of retained Fourier modes is initially selected as 16, 32, and 64, while the depth of P and Q is chosen from 32, 64, and 128. We consider learning rates of 0.001 and 0.0005. The results of the tuning process are presented in Table B2. The optimal model is selected with four Fourier layers, 32 Fourier modes, 128 neurons in P and Q , and a learning rate of 0.001.

Table B2. Relative L_2 errors for different hyperparameter configurations, including the number of Fourier layers, modes, learning rate, and the widths of P and Q , tested on data from a 3D simulation of dynamic rupture.

Learning Rate	Modes	Width of P and Q		
		32	64	128
0.001	16	0.127383	0.115418	0.113272
	32	0.108283	0.105937	0.080965
	64	0.102793	0.126559	0.114296
0.0005	16	0.123509	0.093694	0.107529
	32	0.101131	0.096700	0.083106
	64	0.096357	0.106043	0.091511

Open Research

All data used in the analysis are available online at Tainpakdipat et al. (2025). The FNO software used to conduct the numerical experiments will be made available upon acceptance.

612 **Acknowledgments**

613 The study was supported by the National Science Foundation (CAREER award No. 1753249
614 and OAC-2311207) and the Southern/Statewide California Earthquake Center (based
615 on NSF Cooperative Agreement EAR-1600087 and USGS Cooperative Agreement G17AC00047).
616 We also acknowledge funding provided by DOE EERE Geothermal Technologies Office
617 to Utah FORGE and the University of Utah under Project DE-EE0007080 Enhanced
618 Geothermal System Concept Testing and Development at the Milford City, Utah Fron-
619 tier Observatory for Research in Geothermal Energy (Utah FORGE) site.

620 **References**

- 621 Aagaard, B. T., Heaton, T. H., & Hall, J. F. (2001). Dynamic earthquake ruptures
622 in the presence of lithostatic normal stresses: Implications for friction models
623 and heat production. *Bulletin of the Seismological Society of America*, 91(6),
624 1765–1796.
- 625 Abdelmeguid, M., & Elbanna, A. (2022). Modeling sequences of earthquakes and
626 aseismic slip (seas) in elasto-plastic fault zones with a hybrid finite element
627 spectral boundary integral scheme. *Journal of Geophysical Research: Solid*
628 *Earth*, 127(12), e2022JB024548.
- 629 Abdelmeguid, M., Ma, X., & Elbanna, A. (2019). A novel hybrid finite element-
630 spectral boundary integral scheme for modeling earthquake cycles: Application
631 to rate and state faults with low-velocity zones. *Journal of Geophysical Re-*
632 *search: Solid Earth*, 124(12), 12854–12881.
- 633 Ampuero, J.-P., & Rubin, A. M. (2008). Earthquake nucleation on rate and state
634 faults—aging and slip laws. *Journal of Geophysical Research: Solid Earth*,
635 113(B1).
- 636 Andrews, D. (1973). A numerical study of tectonic stress release by underground ex-
637 plosions. *Bulletin of the Seismological Society of America*, 63(4), 1375–1391.
- 638 Andrews, D. (1980). A stochastic fault model: 1. static case. *Journal of Geophysical*
639 *Research: Solid Earth*, 85(B7), 3867–3877.
- 640 Andrews, D. (1985). Dynamic plane-strain shear rupture with a slip-weakening fric-
641 tion law calculated by a boundary integral method. *Bulletin of the Seismologi-*
642 *cal Society of America*, 75(1), 1–21.
- 643 Andrews, D. (1999). Test of two methods for faulting in finite-difference calculations.
644 *Bulletin of the Seismological Society of America*, 89(4), 931–937.
- 645 Aochi, H., & Twardzik, C. (2020). Imaging of seismogenic asperities of the 2016 ml
646 6.0 amatrice, central italy, earthquake through dynamic rupture simulations.
647 *Pure and Applied Geophysics*, 177(5), 1931–1946.
- 648 Arrowsmith, S. J., Trugman, D. T., MacCarthy, J., Bergen, K. J., Lumley, D., &
649 Magnani, M. B. (2022). Big data seismology. *Reviews of Geophysics*, 60(2),
650 e2021RG000769.
- 651 Azizzadenesheli, K., Kovachki, N., Li, Z., Liu-Schiavini, M., Kossaifi, J., & Anand-
652 kumar, A. (2024). Neural operators for accelerating scientific simulations and
653 design. *Nature Reviews Physics*, 6(5), 320–328.
- 654 Barall, M., & Harris, R. A. (2015). Metrics for comparing dynamic earthquake rup-
655 ture simulations. *Seismological Research Letters*, 86(1), 223–235.
- 656 Ben-Zion, Y. (2008). Collective behavior of earthquakes and faults: Continuum-
657 discrete transitions, progressive evolutionary changes, and different dynamic
658 regimes. *Reviews of Geophysics*, 46(4).
- 659 Ben-Zion, Y., & Rice, J. R. (1997). Dynamic simulations of slip on a smooth fault
660 in an elastic solid. *Journal of Geophysical Research: Solid Earth*, 102(B8),
661 17771–17784.
- 662 Bhat, H. S., Olives, M., Dworska, R., & Rice, J. R. (2007). Role of fault branches
663 in earthquake rupture dynamics. *Journal of Geophysical Research: Solid Earth*,
664 112(B11).

- 665 Cao, Y., Fang, Z., Wu, Y., Zhou, D.-X., & Gu, Q. (2019). Towards understanding
666 the spectral bias of deep learning. *arXiv preprint arXiv:1912.01198*.
- 667 Chester, F. M., & Chester, J. S. (1998). Ultracataclasite structure and friction pro-
668 cesses of the punchbowl fault, san andreas system, california. *Tectonophysics*,
669 295(1-2), 199–221.
- 670 Cochard, A., & Madariaga, R. (1994). Dynamic faulting under rate-dependent fric-
671 tion. *pure and applied geophysics*, 142(3), 419–445.
- 672 Cuomo, S., Di Cola, V. S., Giampaolo, F., Rozza, G., Raissi, M., & Piccialli, F.
673 (2022). Scientific machine learning through physics-informed neural networks:
674 Where we are and what's next. *Journal of Scientific Computing*, 92(3), 88.
- 675 Dalguer, L. A., & Day, S. M. (2007). Staggered-grid split-node method for spon-
676 taneous rupture simulation. *Journal of Geophysical Research: Solid Earth*,
677 112(B2).
- 678 Das, S. (1980). A numerical method for determination of source time functions for
679 general three-dimensional rupture propagation. *Geophysical Journal Interna-
680 tional*, 62(3), 591–604.
- 681 Day, S. M. (1982). Three-dimensional finite difference simulation of fault dynamics:
682 rectangular faults with fixed rupture velocity. *Bulletin of the Seismological So-
683 ciety of America*, 72(3), 705–727.
- 684 de Hoop, M. V., Huang, D. Z., Qian, E., & Stuart, A. M. (2022). The cost-
685 accuracy trade-off in operator learning with neural networks. *arXiv preprint
686 arXiv:2203.13181*.
- 687 Dieterich, J. H. (1979). Modeling of rock friction: 1. experimental results and consti-
688 tutive equations. *Journal of Geophysical Research: Solid Earth*, 84(B5), 2161–
689 2168.
- 690 Duan, B., & Oglesby, D. D. (2006). Heterogeneous fault stresses from previous
691 earthquakes and the effect on dynamics of parallel strike-slip faults. *Journal of
692 Geophysical Research: Solid Earth*, 111(B5).
- 693 Gabriel, A.-A., Ampuero, J.-P., Dalguer, L., & Mai, P. M. (2012). The transition
694 of dynamic rupture styles in elastic media under velocity-weakening friction.
695 *Journal of Geophysical Research: Solid Earth*, 117(B9).
- 696 Gallovič, F., Valentová, Ľ., Ampuero, J.-P., & Gabriel, A.-A. (2019a). Bayesian
697 Dynamic Finite-Fault Inversion: 1. Method and Synthetic Test. *Journal
698 of Geophysical Research: Solid Earth*, 124(7), 6949–6969. doi: 10.1029/
699 2019JB017510
- 700 Gallovič, F., Valentová, L., Ampuero, J.-P., & Gabriel, A.-A. (2019b). Bayesian dy-
701 namic finite-fault inversion: 2. application to the 2016 mw 6.2 amatrice, italy,
702 earthquake. *Journal of Geophysical Research: Solid Earth*, 124(7), 6970–6988.
- 703 Geubelle, P. H., & Rice, J. R. (1995). A spectral method for three-dimensional elas-
704 todynamic fracture problems. *Journal of the Mechanics and Physics of Solids*,
705 43(11), 1791–1824.
- 706 Harris, R. A., Barall, M., Aagaard, B., Ma, S., Roten, D., Olsen, K., ... others
707 (2018). A suite of exercises for verifying dynamic earthquake rupture codes.
708 *Seismological Research Letters*, 89(3), 1146–1162.
- 709 Harris, R. A., Barall, M., Archuleta, R., Dunham, E., Aagaard, B., Ampuero, J. P.,
710 ... others (2009). The scec/usgs dynamic earthquake rupture code verification
711 exercise. *Seismological Research Letters*, 80(1), 119–126.
- 712 Hendrycks, D., & Gimpel, K. (2016). Gaussian error linear units (gelus). *arXiv
713 preprint arXiv:1606.08415*.
- 714 Hirata, T. (1989). A correlation between the b value and the fractal dimension
715 of earthquakes. *Journal of Geophysical Research: Solid Earth*, 94(B6), 7507–
716 7514.
- 717 Ikari, M. J., Marone, C., & Saffer, D. M. (2011). On the relation between fault
718 strength and frictional stability. *Geology*, 39(1), 83–86.
- 719 Johnson, K. M., Burgmann, R., & Larson, K. (2006). Frictional properties on the

- 720 san andreas fault near parkfield, california, inferred from models of afterslip
721 following the 2004 earthquake. *Bulletin of the Seismological Society of Amer-*
722 *ica*, 96(4B), S321–S338.
- 723 Kammer, D. S., Albertini, G., & Ke, C.-Y. (2021). Uguca: A spectral-boundary-
724 integral method for modeling fracture and friction. *SoftwareX*, 15, 100785.
- 725 Kingma, D. P., & Ba, J. (2014). Adam: A method for stochastic optimization. *arXiv*
726 *preprint arXiv:1412.6980*.
- 727 Kong, Q., Zou, C., Choi, Y., Matzel, E. M., Azizzadenesheli, K., Ross, Z. E., ...
728 Clayton, R. W. (2025). Reducing frequency bias of fourier neural operators in
729 3d seismic wavefield simulations through multi-stage training. *arXiv preprint*
730 *arXiv:2503.02023*.
- 731 Kovachki, N., Li, Z., Liu, B., Azizzadenesheli, K., Bhattacharya, K., Stuart, A., &
732 Anandkumar, A. (2023). Neural operator: Learning maps between function
733 spaces with applications to pdes. *Journal of Machine Learning Research*,
734 24(89), 1–97.
- 735 Lapusta, N., Rice, J. R., Ben-Zion, Y., & Zheng, G. (2000). Elastodynamic analysis
736 for slow tectonic loading with spontaneous rupture episodes on faults with
737 rate-and state-dependent friction. *Journal of Geophysical Research: Solid*
738 *Earth*, 105(B10), 23765–23789.
- 739 Lehmann, F., Gatti, F., Bertin, M., & Clouteau, D. (2023). Fourier neural oper-
740 ator surrogate model to predict 3d seismic waves propagation. *arXiv preprint*
741 *arXiv:2304.10242*.
- 742 Lehmann, F., Gatti, F., Bertin, M., & Clouteau, D. (2024). 3d elastic wave prop-
743 agation with a factorized fourier neural operator (f-fno). *Computer Methods in*
744 *Applied Mechanics and Engineering*, 420, 116718.
- 745 Li, B., Wang, H., Feng, S., Yang, X., & Lin, Y. (2023). Solving seismic wave equa-
746 tions on variable velocity models with fourier neural operator. *IEEE Transac-*
747 *tions on Geoscience and Remote Sensing*, 61, 1–18.
- 748 Li, Z., Kovachki, N., Azizzadenesheli, K., Liu, B., Bhattacharya, K., Stuart, A.,
749 & Anandkumar, A. (2020). Fourier neural operator for parametric partial
750 differential equations. *arXiv preprint arXiv:2010.08895*.
- 751 Ma, X., & Elbanna, A. (2019). Dynamic rupture propagation on fault planes with
752 explicit representation of short branches. *Earth and Planetary Science Letters*,
753 523, 115702.
- 754 Ma, X., Hajarolasvadi, S., Albertini, G., Kammer, D. S., & Elbanna, A. E. (2019).
755 A hybrid finite element-spectral boundary integral approach: Applications to
756 dynamic rupture modeling in unbounded domains. *International Journal for*
757 *Numerical and Analytical Methods in Geomechanics*, 43(1), 317–338.
- 758 Madariaga, R., Olsen, K., & Archuleta, R. (1998). Modeling dynamic rupture in
759 a 3d earthquake fault model. *Bulletin of the Seismological Society of America*,
760 88(5), 1182–1197.
- 761 Moczo, P., Kristek, J., Galis, M., Pazak, P., & Balazovjech, M. (2007). The finite-
762 difference and finite-element modeling of seismic wave propagation and earth-
763 quake motion. *Acta physica slovaca*, 57(2).
- 764 Mousavi, S. M., Ellsworth, W. L., Zhu, W., Chuang, L. Y., & Beroza, G. C. (2020).
765 Earthquake transformer—an attentive deep-learning model for simultaneous
766 earthquake detection and phase picking. *Nature communications*, 11(1), 3952.
- 767 Nielsen, S. B., Carlson, J., & Olsen, K. B. (2000). Influence of friction and fault ge-
768 ometry on earthquake rupture. *Journal of Geophysical Research: Solid Earth*,
769 105(B3), 6069–6088.
- 770 Oglesby, D. D., Archuleta, R. J., & Nielsen, S. B. (1998). Earthquakes on dipping
771 faults: The effects of broken symmetry. *Science*, 280(5366), 1055–1059.
- 772 Oglesby, D. D., Archuleta, R. J., & Nielsen, S. B. (2000). The three-dimensional
773 dynamics of dipping faults. *Bulletin of the Seismological Society of America*,
774 90(3), 616–628.

- 775 Rahaman, N., Baratin, A., Arpit, D., Draxler, F., Lin, M., Hamprecht, F., ...
776 Courville, A. (2019). On the spectral bias of neural networks. In *International*
777 *conference on machine learning* (pp. 5301–5310).
- 778 Rahman, M. A., Ross, Z. E., & Azizzadenesheli, K. (2022). U-no: U-shaped neural
779 operators. *arXiv preprint arXiv:2204.11127*.
- 780 Renard, F., & Candela, T. (2017). Scaling of fault roughness and implications for
781 earthquake mechanics. *Fault zone dynamic processes: Evolution of fault proper-*
782 *ties during seismic rupture*, 195–215.
- 783 Ripperger, J., Ampuero, J.-P., Mai, P., & Giardini, D. (2007). Earthquake source
784 characteristics from dynamic rupture with constrained stochastic fault stress.
785 *Journal of Geophysical Research: Solid Earth*, 112(B4).
- 786 Ross, Z. E., Meier, M.-A., & Hauksson, E. (2018). P wave arrival picking and first-
787 motion polarity determination with deep learning. *Journal of Geophysical Re-*
788 *search: Solid Earth*, 123(6), 5120–5129.
- 789 Ross, Z. E., Yue, Y., Meier, M.-A., Hauksson, E., & Heaton, T. H. (2019).
790 Phaselink: A deep learning approach to seismic phase association. *Journal*
791 *of Geophysical Research: Solid Earth*, 124(1), 856–869.
- 792 Ruina, A. (1983). Slip instability and state variable friction laws. *Journal of Geo-*
793 *physical Research: Solid Earth*, 88(B12), 10359–10370.
- 794 Tainpkdipat, N., Abdelmeguid, M., Zhao, C., & Elbanna, A. (2025). *Fourier neural*
795 *operators for accelerating earthquake dynamic rupture simulations* [data set].
796 Zenodo. Retrieved from <https://doi.org/10.5281/zenodo.15085622> doi:
797 10.5281/zenodo.15085622
- 798 Ulrich, T., Gabriel, A.-A., Ampuero, J.-P., & Xu, W. (2019). Dynamic viability
799 of the 2016 mw 7.8 kaikōura earthquake cascade on weak crustal faults. *Nature*
800 *Communications*, 10, 1213. doi: 10.1038/s41467-019-09125-w
- 801 Van Zelst, I., Wollherr, S., Gabriel, A.-A., Madden, E. H., & van Dinther, Y. (2019).
802 Modeling megathrust earthquakes across scales: One-way coupling from geo-
803 dynamics and seismic cycles to dynamic rupture. *Journal of Geophysical*
804 *Research: Solid Earth*, 124(11), 11414–11446.
- 805 Wei, W., & Fu, L.-Y. (2022). Small-data-driven fast seismic simulations for com-
806 plex media using physics-informed fourier neural operators. *Geophysics*, 87(6),
807 T435–T446.
- 808 Xu, J., Zhang, H., & Chen, X. (2015). Rupture phase diagrams for a planar fault in
809 3-d full-space and half-space. *Geophysical Journal International*, 202(3), 2194–
810 2206.
- 811 Yang, L., Liu, X., Zhu, W., Zhao, L., & Beroza, G. C. (2022). Toward improved ur-
812 ban earthquake monitoring through deep-learning-based noise suppression. *Sci-*
813 *ence advances*, 8(15), eabl3564.
- 814 Yang, Y., Gao, A. F., Azizzadenesheli, K., Clayton, R. W., & Ross, Z. E. (2023).
815 Rapid seismic waveform modeling and inversion with neural operators. *IEEE*
816 *Transactions on Geoscience and Remote Sensing*, 61, 1–12.
- 817 Yang, Y., Gao, A. F., Castellanos, J. C., Ross, Z. E., Azizzadenesheli, K., & Clay-
818 ton, R. W. (2021). Seismic wave propagation and inversion with neural
819 operators. *The Seismic Record*, 1(3), 126–134.
- 820 Zhang, T., Trad, D., & Innanen, K. (2023). Learning to solve the elastic wave equa-
821 tion with fourier neural operators. *Geophysics*, 88(3), T101–T119.
- 822 Zhu, W., & Beroza, G. C. (2019). Phasenet: a deep-neural-network-based seismic
823 arrival-time picking method. *Geophysical Journal International*, 216(1), 261–
824 273.
- 825 Zhu, W., Mousavi, S. M., & Beroza, G. C. (2019). Seismic signal denoising and
826 decomposition using deep neural networks. *IEEE Transactions on Geoscience*
827 *and Remote Sensing*, 57(11), 9476–9488.
- 828 Zhu, W., Tai, K. S., Mousavi, S. M., Bailis, P., & Beroza, G. C. (2022). An end-
829 to-end earthquake detection method for joint phase picking and association

- 830 using deep learning. *Journal of Geophysical Research: Solid Earth*, 127(3),
831 e2021JB023283.
- 832 Zou, C., Azizzadenesheli, K., Ross, Z. E., & Clayton, R. W. (2024). Deep neural
833 helmholtz operators for 3d elastic wave propagation and inversion. *Geophysical*
834 *Journal International*, ggae342.